JOURNAL PRE-PROOF

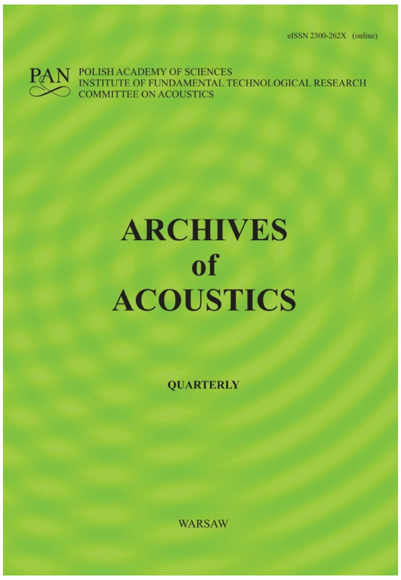

eISSN 2300-262X (online)

PAN POLISH ACADEMY OF SCIENCES
INSTITUTE OF FUNDAMENTAL TECHNOLOGICAL RESEARCH
COMMITTEE ON ACOUSTICS

ARCHIVES
of
ACOUSTICS

QUARTERLY

WARSAW

Title: Study on Dual-Stage Amplification Cascaded Piezoelectric Transducer for High-Power Applications

Author(s): Guo Li, Peiyu Tan, Ruihui Ma, Feilong Li, Xiaoli Zhang, Hua Tian

DOI: https://doi.org/10.24423/archacoust.2026.4275
Journal: *Archives of Acoustics*
ISSN: 0137-5075, e-ISSN: 2300-262X
Publication status: In press
Received: 2025-07-10
Revised: 2025-12-25
Accepted: 2026-01-01
Published pre-proof: 2026-01-15

Please cite this article as:

Li G., Tan P., Ma R., Li F., Zhang X., Tian H. (2026), Study on Dual-Stage Amplification Cascaded Piezoelectric Transducer for High-Power Applications, *Archives of Acoustics*, https://doi.org/10.24423/archacoust.2026.4275

Study on Dual-Stage Amplification Cascaded Piezoelectric Transducer for High-Power Applications

Guo Li[1*], Peiyu Tan[1], Ruihui Ma[1], Feilong Li[1], Xiaoli Zhang[2], Hua Tian[3]

[1] School of Automation, Xi'an Key Laboratory of Advanced Control and Intelligent Processing, Xi'an University of Posts &Telecommunications, Xi'an, China

[2]Department of Electronic & Information Engineering,
Ankang University, Ankang, Shaanxi, China

[3]Key Laboratory of Ultrasound of Shaanxi Province, School of Physics and Information Technology, Shaanxi Normal University, Xi'an, China

*Corresponding Author: liguo@xupt.edu.cn

To reduce the size and enhance the efficiency of cascaded sandwich transducers with conical horns, a novel structural configuration of such transducers was investigated. This transducer incorporates two sets of piezoelectric stacks, enabling two-stage amplification for improved efficiency. An equivalent circuit model for the cascaded sandwich transducer with a conical horn was established, systematically deriving analytical expressions for core performance parameters including input impedance, velocity amplification ratio, and resonant characteristics. Through theoretical and simulation analyses, the dynamic influence of key structural parameters on electromechanical energy conversion efficiency was determined, specifically the output radius of the second-stage, the relative position of the variable cross-section of two sets of piezoelectric ceramic sandwich structures, and the spacing between the two sets of piezoelectric ceramics. Furthermore, a performance optimization strategy based on piezoelectric single-crystal materials was proposed. Numerical simulations validated against theoretical models revealed the governing principles of piezoelectric materials on transducer performance. Experimental results demonstrate excellent agreement between the operational characteristics of the optimized transducer and predictions from both theoretical models and finite element simulations. This work holds guiding significance for optimizing multi-mode transducers and demonstrates promising application potential in high-power ultrasonic fields.

Keywords: cascaded transducer; multi-mode; velocity amplification ratio; finite element analysis.

1. Introduction

In recent years, power ultrasonic technology has demonstrated extensive application prospects across diverse fields including ultrasonic machining, precision cleaning, underwater acoustics, sonochemistry, food processing, and biodiesel production (Shah, Liu, 2019; Tan, Tan, 2022; Li *et al*., 2018; Pokhrel *et al*., 2016; Subhedar, Gogate, 2015; Chemat *et al*., 2011). Particularly in ultrasonic motor research, piezoelectric transducer-based ultrasonic systems have attracted significant scientific attention (Li, Zheng, 2023; Roland, 2024; Jiang *et al*., 2024). As critical components in ultrasonic systems, sandwich piezoelectric ultrasonic transducers exhibit remarkable advantages in electromechanical energy conversion through the piezoelectric effect, featuring simplified structural design, high conversion efficiency, and substantial vibration amplitude, making them predominant in high-power ultrasonic applications (Lin, 2009; Kuang *et al*., 2014; Du *et al*., 2020; Davari *et al*., 2012). Their utility extends to piezoelectric nanopositioning systems and robotic manipulators (Su *et al*., 2018; Jiang *et al*., 2018; Liu *et al*., 2023).

To meet escalating demands in high-power applications, research focus has shifted toward optimizing conventional sandwich transducers and developing novel vibration systems. Enhanced radiation coverage and ultrasonic intensity have been achieved through geometric modifications and vibration mode innovations, leading to proposals for coupled-vibration transducers and mode-conversion composite systems, including longitudinal-torsional, radial-torsional, flexural-torsional, longitudinal-flexural, radial-flexural, and inter-digital configurations (Li *et al*., 2018; Meshkinzar, Al-Jumaily, 2021; Watanabe *et al*., 2021; Lin *et al*., 2011; Lin *et al*., 2013; Li *et al*., 2023; Tressler *et al*., 2006; Lin, 2007; Tang *et al*., 2024; Xu *et al*., 2019; Hunter *et al*., 2019). Lin (2017) pioneered the concept of cascaded piezoelectric transducers, where multiple half-wavelength sandwich transducers synergistically amplify input electrical power and ultrasonic intensity. Subsequent work by Lin et al.(2018) introduced tunable longitudinal transducers with comprehensive performance characterization. Li et al. (2022) conducted multifrequency analysis on stepped conical transducers, deriving equivalent impedance models and frequency resonance equations through theoretical modeling and experimental validation. Cascaded transducers can operate at different resonant frequencies to meet the requirements of multi frequency modes. This cascaded vibration structure can also double the power and intensity of ultrasonic waves, and the intermediate mass block can assist in heat dissipation.However, systematic investigation into the multimodal vibration characteristics—crucial for optimizing energy transfer and operational stability—of conical cascaded sandwich transducers remains limited. Specifically, the correlations between their multi-frequency performance and key geometric parameters are not well understood, hindering their optimized design for high-power, multi-mode applications."

To address this gap, this study investigates the relationship between the performance parameters, geometric dimensions, and piezoelectric materials of a conical cascaded sandwich piezoelectric transducer in multi frequency mode. A theoretical analysis model was established based on the derivation of the frequency equation and vibration velocity amplification ratio expression for cascaded transducers using Kirchhoff's law. Keeping the conical amplitude rod structure unchanged, the geometric dimensions of the piezoelectric stack radius near the output end of the amplitude rod and the spatial configuration of the sandwich structure of the two piezoelectric stacks were changed, and the piezoelectric material PZT-8 was replaced with a relaxor ferroelectric single crystal. The impact of using PZT-8 in combination with relaxor ferroelectric single crystal on vibration performance was analyzed, and the changes in performance parameters were analyzed using theoretical models and numerical simulations. Based on theoretical and simulation results, an optimized transducer prototype was manufactured and experimentally tested. The results are in good agreement with the predictions and validate the proposed design method. This work provides a practical optimization framework for cascaded transducers with cone horn, which has important guiding value for the development of efficient and high-power ultrasound systems in precision machining, sonochemistry, and other applications.

2. Theoretical analysis

The ultrasonic composite transducer is formed by the longitudinal cascade of two sandwich-type structures, a conical horn, and a prestressed bolt. These two sandwich structures serve as two-stage excitation mechanisms. In the design, the influence of the bolt prestress is neglected; consequently, the two sandwich structures and the conical horn can be considered as a solid rod bonded together. Fig. 1 illustrates the structural diagram of the ultrasonic transducer, comprising seven components: back metal cylinder I, piezoelectric stack II, middle metal cylinder III, middle metal cylinder IV, piezoelectric stack V, front metal cylinder VI, and cone horn VII. The parameter L_i (i=1, 2, 3, 4, 5, 6, 7)corresponds to the length of each component, while the parameter R_i (i=1, 2, 3, 4, 5, 6, 7) corresponds to the cross-sectional radius of each component, N_i (i=1, 2) represents the electromechanical conversion coefficient of piezoelectric ceramic stack.

The equivalent circuit diagram of the transducer is presented in Fig. 2. Here, V denotes the excitation voltage, I_1 and I_2 represent the currents entering the two piezoelectric stacks, respectively. v_i (I = 1, 2, 3, 4, 5, 6) signifies the vibration velocity at each designated section, while v_b and v_f denote the longitudinal vibration velocities on the outer surfaces of the rear metal cylinder and the conical horn, respectively. C_i represents the clamped capacitance of the piezoelectric stacks, n_i is the electromechanical transformation ratio, p is the number of piezoelectric rings, ρ is the density, E is Young's modulus, k is the wavenumber, and c is the longitudinal wave sound velocity. Z_{i1}、Z_{i2}、Z_{i3} (i=1, 2, 3, 4, 5, 6, 7) denote the impedances of the metal cylinders and piezoelectric ceramic stacks, respectively, where $Z_{i1} = Z_{i2} = jZ_{0i}\tan(\frac{k_i L_i}{2}),\ Z_{i3} = \frac{Z_{0i}}{j\sin(k_i L_i)}$.

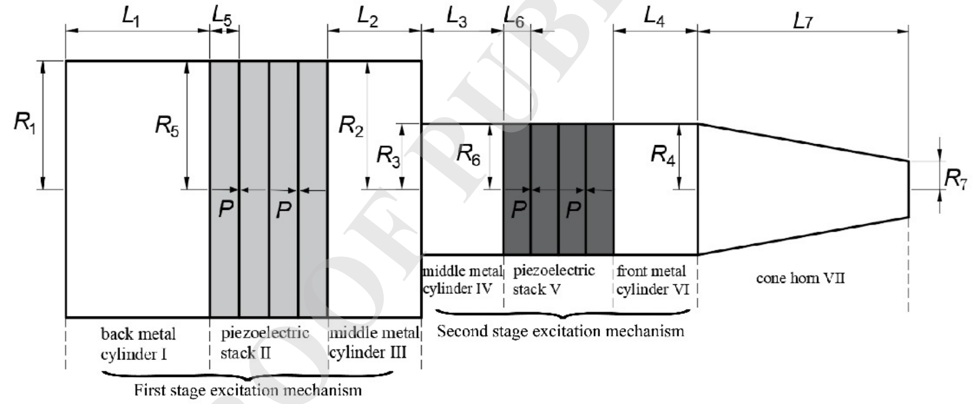

Fig. 1. Structural diagram of the cascaded excitation longitudinal output system

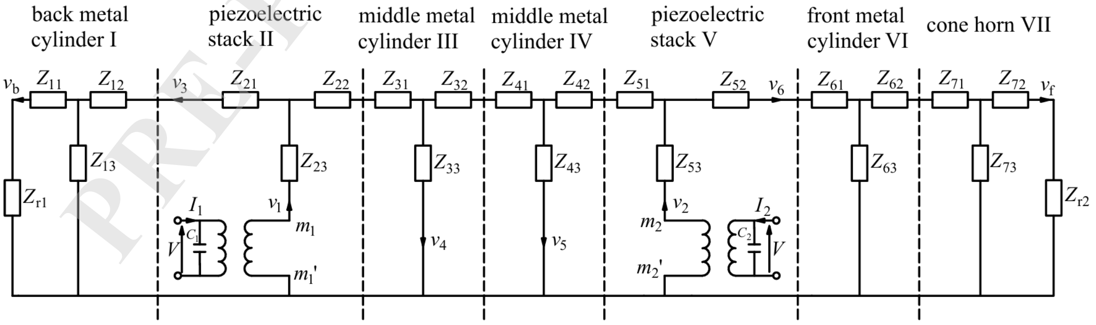

Fig. 2. Equivalent circuit of the cascaded excitation longitudinal output system

Li et al. (2024) conducted research on the equivalent circuit. From this model, the mechanical impedances Z_{m1} and Z_{m2} between the mechanical terminals m_1, m_1' and m_2, m_2' can be obtained, leading to the derivation of the total equivalent mechanical impedance Z_{m},

$$Z_{m1} = Z_{23} + \frac{v_3}{v_1}\left[\frac{\left(Z_{r1}+Z_{11}\right)Z_{13}}{\left(Z_{r1}+Z_{11}\right)+Z_{13}} + Z_{12} + Z_{21} \right] \tag{1}$$

$$Z_{m2} = Z_{53} + \frac{v_6}{v_2}\left[\frac{(Z_{71}+Z_{62})(Z_{72}+Z_{73})Z_{32}+Z_{72}Z_{73}}{(Z_{71}+Z_{62}+Z_{63})(Z_{72}+Z_{73})+Z_{72}Z_{73}} + Z_{61} + Z_{52} \right] \tag{2}$$

Table 1 .The characteristic parameters of the transducer.

Material	ρ (kg/m^3)	E (N/m^2)	v	s^{E}_{33} (m^2/N)	d_{33} (C/N)	ε^{T}_{33} (C^2/(Nm^2))	k_{33}
40Cr Steel	7840	20.9×10^{10}	0.28				
Duralumin	2790	7.15×10^{10}	0.34				
PZT-8	7600			13.9×10^{-12}	225×10^{-12}	8.84×10^{-9}	0.62
single crystal	8122			49×10^{-12}	1285×10^{-12}	42.1×10^{-9}	0.87

$$Z_m = \frac{Z_{m1}Z_{m2}}{Z_{m1}(jwC_2Z_{m2}+N_2^2)+Z_{m2}(jwC_1Z_{m1}+N_1^2)} \tag{3}$$

Among which, $w=2\pi f$, f is the frequency.

The resonant frequency f_{r} is calculated when Z_{m} approaches zero, and the anti-resonant frequency f_{a} is calculated when Z_{m} approaches infinity. The effective electromechanical coupling coefficient is $k_{eff} = \sqrt{(1-(\frac{f_r}{f_a})^2)}$, and the velocity amplitude magnification ratio is $M = \left|\frac{v_b}{v_f}\right|$.

3. Relationships between performance parameters and geometric dimensions of the cascaded piezoelectric transducer with cone horn

To investigate the influence of the transducer structure's geometric dimensions on its performance, the metal block material is 40Cr steel, while other metal blocks and the conical metal component are made of hard aluminum. The piezoelectric materials employed are PZT-8 and relaxor ferroelectric single crystal. PZT-8 is widely utilized in ultrasonic transducer research due to its advantageous properties, including a high electromechanical coupling coefficient, high mechanical strength, and fast response speed. Compared to PZT-8, relaxor ferroelectric single crystal exhibits higher piezoelectric and dielectric constants along with lower dielectric loss, making it the preferred material for high-precision ultrasonic applications. Their typical characteristic parameters are listed in Table 1. Through theoretical analysis, the function of impedance with respect to frequency can be obtained. By assigning a value to the frequency, the impedance value can be obtained, and the impedance curve can be obtained. From the curve, the resonant and anti resonant frequencies can be obtained, and the electromechanical coupling coefficient can be calculated. By substituting the resonant frequency into the amplification ratio formula, the amplification ratio can be calculated. This theoretical calculation process is implemented using Matlab. These performance parameters were also obtained through numerical simulation using ANSYS. The model was established in an axisymmetric configuration. The metal components were discretized with PLANE42 elements, a 4-node axisymmetric structural solid element suitable for linear elastic analysis. The piezoelectric ceramic stacks were modeled using PLANE13 elements, a 4-node axisymmetric coupled-field solid element that can directly solve the interaction between electrical and mechanical degrees of freedom. Free meshing with a node size of 0.001 was applied to each part of the transducer. The effects of pre-tightening bolt stress and structural constraints were neglected during the simulation.

3.1 The influence of output radius of the second stage on performance parameters

Using PZT-8 as the piezoelectric material, the initial dimensional parameters of the transducer are: L_1=0.02m, L_2=L_3=0.0075m, L_4=0.021m, L_5= L_6= 0.005 m, L_7 = 0.054m, R_1= R_2= R_3= R_4= 0.0255 m, R_5= R_6= 0.025m, R_7= 0.009m, p_1= p_2 = 4, τ_1=R_2. The relationship between the performance parameters and the output radius of the second-stage is shown in Fig. 3-Fig. 5，where the subscripts denote: t for theoretical values, s for simulated values, r for resonance, a for anti-resonance, and the numerical suffix i (i=1，2，3) for the first three longitudinal vibration modes. Thus, for example, For example, f_{tr1} refers to the theoretical fundamental resonant frequency, f_{sa2} refers to the simulated second anti - resonant frequency, k_{t1} refers to the theoretical first-order effective electromechanical coupling coefficient, k_{s2} refers to the simulated second-order effective electromechanical coupling coefficient, M_{t1} refers to the theoretical first-order velocity amplitude magnification, and M_{s2} refers to the simulated second-order velocity amplitude magnification.

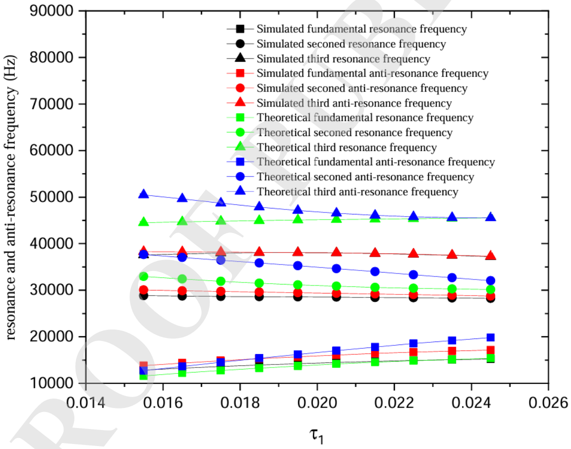

Fig. 3. Relationship between the resonance/anti-resonance frequency and τ_1.

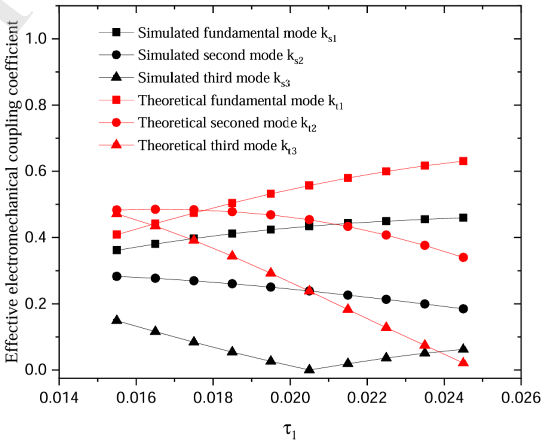

Fig. 4. Relationship between the effective electromechanical coupling coefficient and τ_1.

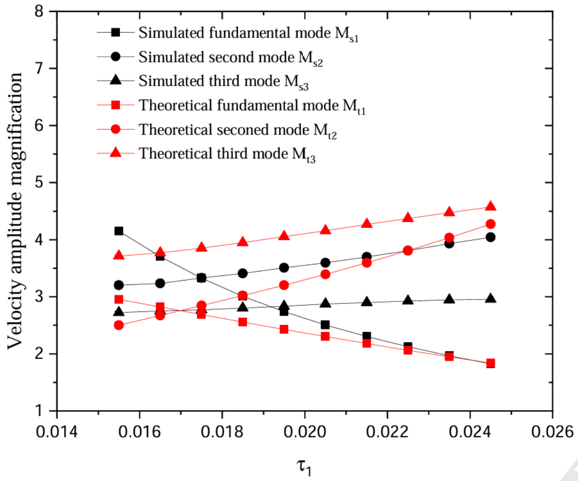

Fig. 5. Relationship between the velocity amplitude magnification and τ_1.

Fig. 3 shows that as the τ_1 increases, the first-order longitudinal vibration resonant and anti-resonant frequencies both increase, while the second-order longitudinal vibration resonant and anti-resonant frequencies decrease. For the third-order longitudinal vibration, the resonant frequency increases while the anti-resonant frequency decreases. In Fig. 4, the first-order longitudinal vibration electromechanical coupling coefficient increases, whereas the effective electromechanical coupling coefficients of the second- and third-order longitudinal vibrations exhibit decreasing trends. Within smaller radius ranges, both first- and second-order longitudinal vibrations maintain relatively large effective electromechanical coupling coefficients, with the third-order coupling coefficient simulation results showing a distinct minimum. Fig. 5 indicates that the first-order longitudinal vibration velocity amplification ratio decreases with increasing R_2, while the second- and third-order velocity amplification ratios increase proportionally. When τ_1 reaches approximately 20.5 mm, the transducer simultaneously achieves large effective electromechanical coupling coefficients and velocity amplification ratios for the first two longitudinal vibration modes, establishing this as the optimized radius for the right-side sandwich-type piezoelectric stack. Therefore, R_3=R_4=0.0205 m and R_6=0.02 m were selected as the dimensional optimization results.

3.2 The influence of the relative position of the variable cross-section of two sets of piezoelectric ceramic sandwich structures on performance parameters

According to the above section, keep the radius of the metal block and piezoelectric ceramic unchanged. When the length of L_2 and L_3 changes, but the total length of L_2 and L_3 remains unchanged. The initial dimensional parameters of the transducer are: L_1=0.02m, L_2=L_3=0.0075m, L_4=0.021m, L_5 = L_6 = 0.005 m, L_7= 0.054m, R_1 =R_2= 0.0255 m, R_3= R_4= 0.0205m, R_5 =0.025m, R_6 =0.02m, R_7= 0.009m, $p_1 = p_2 = 4$, $\tau_2 = L_2/L_3$. The relationship between resonance frequency, anti resonance frequency, effective electromechanical coupling coefficient, velocity amplification ratio, and τ_2 is shown in Fig. 6-Fig. 8.

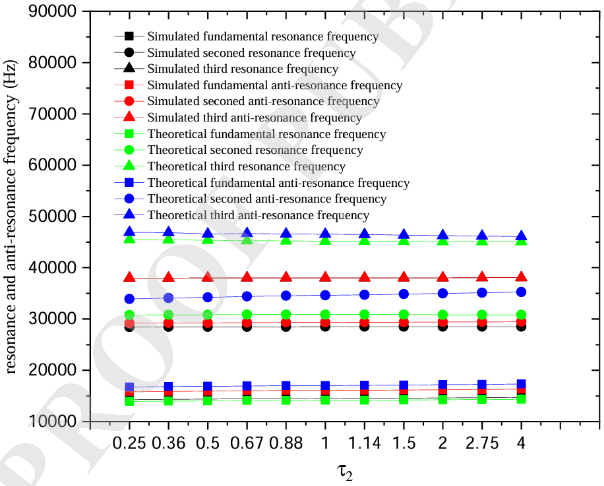

Fig. 6. Relationship between the resonance/anti-resonance frequency and τ_2.

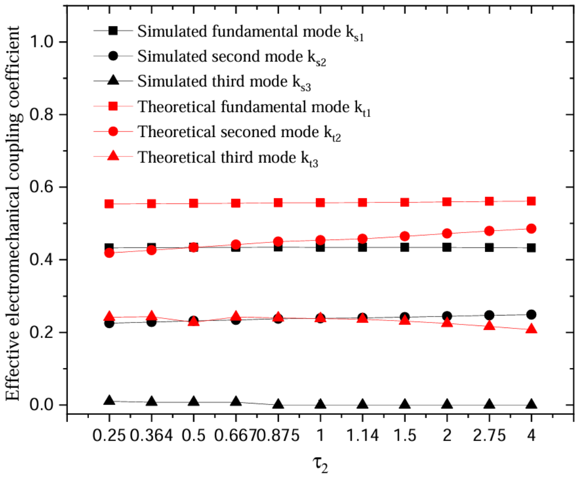

Fig. 7. Relationship between the effective electromechanical coupling coefficient and τ_2.

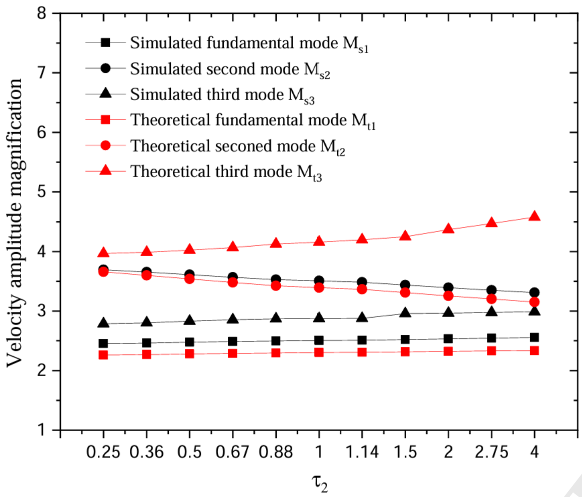

Fig. 8. Relationship between the velocity amplitude magnification and τ_2.

Fig. 6 demonstrates that as τ_2 increases, the resonant and anti-resonant frequencies of the first three longitudinal vibration modes all exhibit gradual increases. In Fig. 7, the electromechanical coupling coefficients of the first- and second-order longitudinal vibrations show slow increases with τ_2, while the third-order longitudinal vibration electromechanical coupling coefficient decreases gradually. The velocity amplification ratios of the first- and third-order longitudinal vibrations rise slowly with τ_2. Fig. 8 reveals a gradual decrease in the second-order longitudinal vibration velocity amplification ratio as τ_2 increases. Overall, the relative position variation of the variable cross-sections in the two sandwich-type piezoelectric stack structures exerts minimal influence on resonant/anti-resonant frequencies, electromechanical coupling coefficients, and amplification ratios. The optimal relative position is determined as τ_2=1 for the variable cross-sections in the two sandwich-type piezoelectric stack structures.

3.3 The influence of spacing between two groups of piezoelectric ceramics on performance parameters

According to the above section, while maintaining the other structural dimensions of the vibration system constant, the spacing between the two sets of piezoelectric ceramics was varied. This spacing corresponds to the length of the middle metal cylinder III and the middle metal cylinder IV. The length changes of these two metal cylinder were identical, while the total length of the transducer remained unchanged. Consequently, the lengths of the back metal cylinder I and the front metal cylinder VI were adjusted correspondingly in response to the changes in the middle metal cylinder III and the middle metal cylinder IV. The initial dimensional parameters of the transducer are: L_1=0.02m, L_2=L_3=0.0075m, L_4=0.021m, $L_5 = L_6$ = 0.005 m, L_7= 0.054m, R_1= R_2=0.0255 m, R_3= R_4=0.0205m, R_5 =0.025m, R_6 =0.02m, R_7= 0.009m, p_1= p_2 = 4, τ_3=L_2+L_3. The relationship between resonance frequency, anti resonance frequency, effective electromechanical coupling coefficient, velocity amplification ratio, and τ_3 is shown in Fig. 9-Fig. 11.

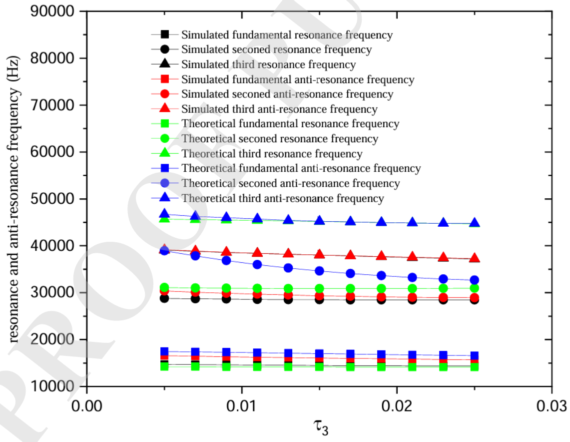

Fig. 9. Relationship between the resonance/anti-resonance frequency and τ_3.

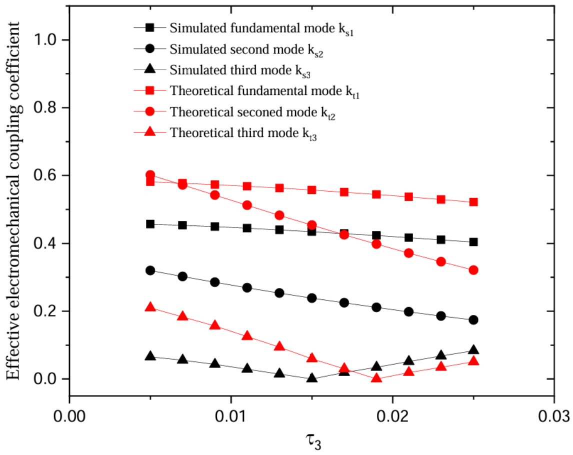

Fig. 10. Relationship between the effective electromechanical coupling coefficient and τ_3.

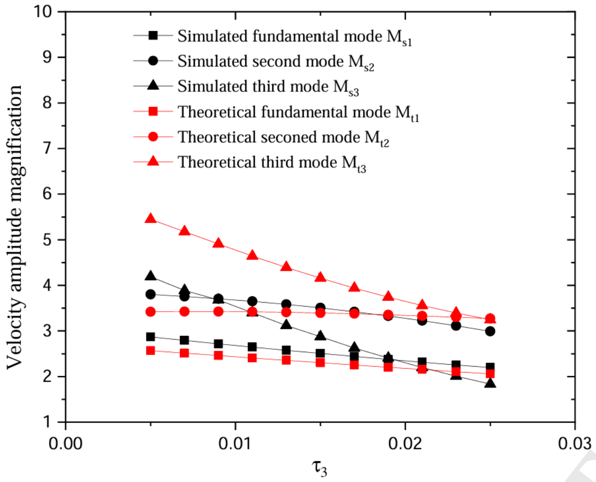

Fig. 11. Relationship between the velocity amplitude magnification and τ_3.

Fig. 9 indicates that as τ_3 increases, the resonant and anti-resonant frequencies of the first three longitudinal vibration modes exhibit gradual decreases. In Fig. 10, the effective electromechanical coupling coefficients of the first- and second-order longitudinal vibrations decrease with increasing τ_3, while the third-order coupling coefficient initially decreases and then increases. Fig. 11 demonstrates that the velocity amplification ratios for all three longitudinal vibration modes decline with larger τ_3, with the first- and second-order modes experiencing smaller reductions compared to the third-order mode. Both theoretical and simulation results collectively indicate that smaller τ_3 between the two piezoelectric stacks enhances the effective electromechanical coupling coefficients and velocity amplification ratios for the first two vibration modes. Considering manufacturing and assembly constraints as well as vibrational coupling intensity between structural components, the piezoelectric ceramic spacing is optimized at 10 mm.

3.4 The influence of piezoelectric materials on performance parameters

Replacing piezoelectric ceramics with relaxor ferroelectric single crystals (RFSCs) alters the transducer's performance, as quantified by theoretical and simulated parameters in Table 2.

The parameters f_{tri}, f_{tai}, f_{sri}, f_{sai}, k_{ti}, k_{si}, M_{ti}, and M_{si} represent theoretical/simulated resonance/anti-resonance frequencies, effective electromechanical coupling coefficients, and velocity amplitude amplification ratios, respectively. Here, i=1, i=2 and i=3 denote configurations with bilateral piezoelectric ceramics, left-side piezoelectric ceramic/right-side RFSC, and bilateral RFSCs. Table 2. demonstrates that replacing the right-side piezoelectric ceramic with an RFSC elevates the first- and third-order electromechanical coupling coefficients but reduces the second-order coupling coefficients, while the amplification ratios exhibit negligible variation. In contrast, substituting both sides with RFSCs induces a pronounced upward trend in all electromechanical coupling coefficients, accompanied by reduced amplification ratios for the first- and second-order modes and an increase in the third-order amplification ratio.

Table 2.

Theoretical and simulated of bilateral piezoelectric ceramics.

Mode	f_{tr1} (Hz)	f_{ta1} (Hz)	f_{sr1} (Hz)	f_{sa1} (Hz)	k_{t1}	k_{s1}	M_{t1}	M_{s1}
Fundamental	14177	17265	14585	16305	0.571	0.447	2.43	2.68
Second	30939	36411	28606	29769	0.527	0.277	3.34	3.68
Third	45453	45883	38481	38506	0.137	0.036	4.77	3.54

Theoretical and simulated of left-side piezoelectric ceramic/right-side RFSC.

Mode	f_{tr2} (Hz)	f_{ta2} (Hz)	f_{sr2} (Hz)	f_{sa2} (Hz)	k_{t2}	k_{s2}	M_{t2}	M_{s2}
Fundamental	12509	18578	11113	15271	0.739	0.686	2.68	2.69
Second	33799	37198	27042	27298	0.418	0.137	3.18	3.37
Third	43554	44996	30577	31366	0.251	0.223	4.78	3.56

Theoretical and simulated of bilateral RFSCs.

Mode	f_{tr3} (Hz)	f_{ta3} (Hz)	f_{sr3} (Hz)	f_{sa3} (Hz)	k_{t3}	k_{s3}	M_{t3}	M_{s3}
Fundamental	8953	14259	10046	14704	0.778	0.730	1.88	1.89
Second	20824	31883	20615	21767	0.757	0.321	1.66	1.77
Third	32740	33469	29647	30690	0.208	0.258	5.72	4.63

Fig. 12-Fig. 14 display the harmonic displacement response from the front to rear radiation surfaces of transducers with three piezoelectric ceramic-relaxor ferroelectric single crystal configurations across the first three vibration modes. When both sides employ

piezoelectric ceramics, symmetrical displacement distributions emerge with lower amplitudes in the first-order mode, while higher modes exhibit progressively amplified vibrations and potential multi-peak displacement patterns. For the asymmetric configuration (left piezoelectric ceramic/right relaxor ferroelectric crystal), the relaxor

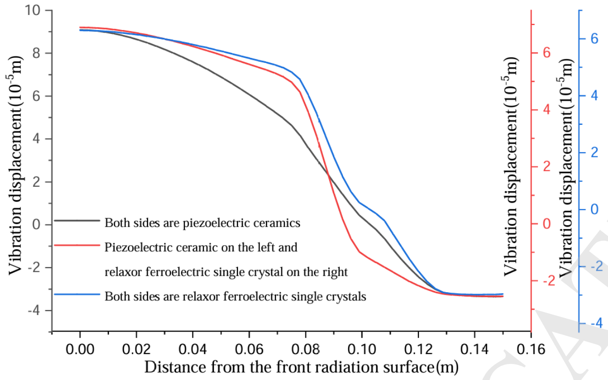

Fig. 12. First order displacement harmonic response curve graph.

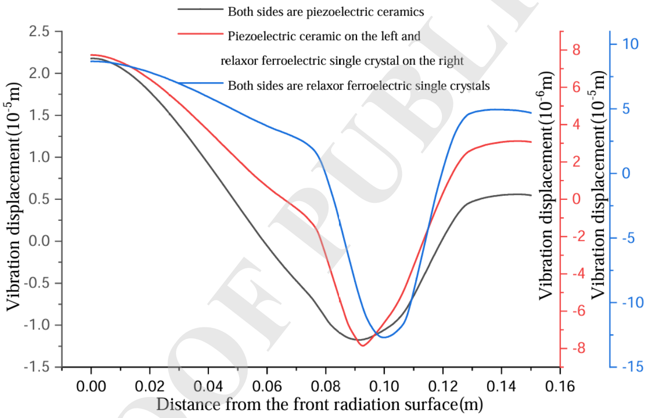

Fig. 13. Second order displacement harmonic response curve graph.

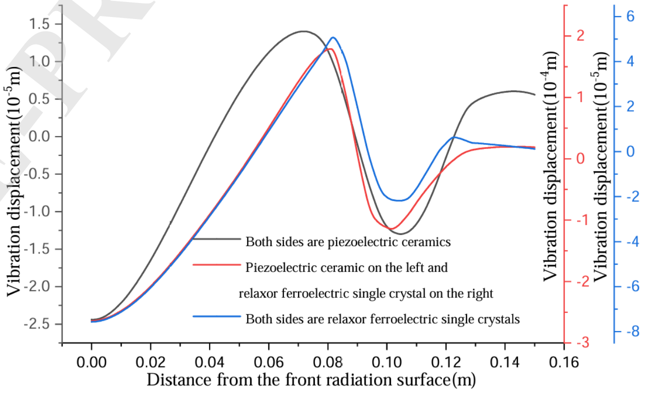

Fig. 14. Third order displacement harmonic response curve graph.

ferroelectric crystal demonstrates localized amplitude enhancement in second and third modes due to its superior mechanical compliance, yet the ceramic's rigidity restricts vibration energy transfer to the rear surface, resulting in insignificant amplification ratio improvement compared to bilateral ceramic configurations. The bilateral relaxor ferroelectric configuration achieves maximum overall vibration amplitudes, where high material compliance promotes efficient energy propagation to the rear surface, generating substantial posterior displacement. Concurrently, reduced wave reflection and increased energy dissipation at the front surface diminish its amplitude, ultimately causing significant degradation of the amplification ratio.

In summary, replacing the right-side piezoelectric ceramic with RFSCs predominantly enhances electromechanical coupling coefficients while minimally affecting amplification ratios, enabling transducers to achieve both high coupling coefficients and velocity amplification at low-order modes. Complete substitution with bilateral RFSCs further optimizes electromechanical coupling performance, demonstrating the material's potential for advanced transducer applications. In practical processes, the size of relaxor ferroelectric single crystals is usually designed to be smaller. The size optimization in this article makes it possible to apply relaxor ferroelectric single crystals to transducers. Compared with piezoelectric ceramics, the performance can be comparable or even superior. In reality, the combination method can be chosen according to the needs.

4. Experiment

Based on the transducer dimensions designed in Section 3, a physical prototype was fabricated and tested. The corresponding structural dimensions are listed in Table 3, while Fig. 15. First Three Mode Shapes illustrates the mode shapes of the transducer under three distinct vibration modes. In this transducer, the capacitors of the left piezoelectric ceramic are 3.414nF, 3.409nF, 3.418nF, and 3.406nF, respectively, and the capacitors of the right piezoelectric ceramic are 1.606nF, 1.625nF, 1.608nF, and 1.635nF, respectively. The total capacitance of the transducer is 20.01nF, indicating good electrical connection.

Table 3. Structural dimensions of the cascaded piezoelectric transducer (unit: mm).

L_1	L_2	L_3	L_4	L_{01}	L_{02}	L_{h1}	R_1	R_2	R_{01}	R_{02}	R_{h1}
22.5	5	5	23.5	5	5	54	25.5	20.5	25	20	9

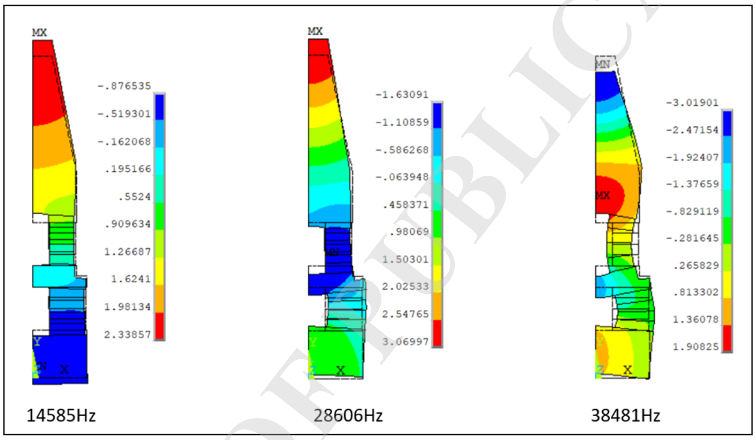

Fig. 15. First Three Mode Shapes

Reactance-frequency responses were acquired using a precision impedance analyzer (E4990A) under 1V excitation across 10-45 kHz. The experimental setup and measured reactance-frequency characteristics are presented in Fig. 16-Fig. 17. Notably, spectral peaks correspond to anti-resonance states while troughs indicate resonance conditions, with the first three resonance points matching the aforementioned vibrational modes. Table 4 provides comparative data of resonance/anti-resonance frequencies obtained through different analytical approaches.

Table 4. Theoretical, simulated and measured frequencies of the multi-frequency mode transducers.

Mode	f_{tr} (Hz)	f_{ta} (Hz)	f_{sr} (Hz)	f_{sa} (Hz)	f_{mr} (Hz)	f_{ma} (Hz)
Fundamental	14177	17265	14585	16305	15187	16660
Second	30939	36411	28606	29769	28367	29343

Third	45453	45883	38481	38506	39418	39549

Fig. 16. (I)Measured the electrical impedance frequency response of the transducer by using the E4990A precision impedance analyzer; (II) Measured the vibration mode of the transducer by using the Polytec scanning vibrator.

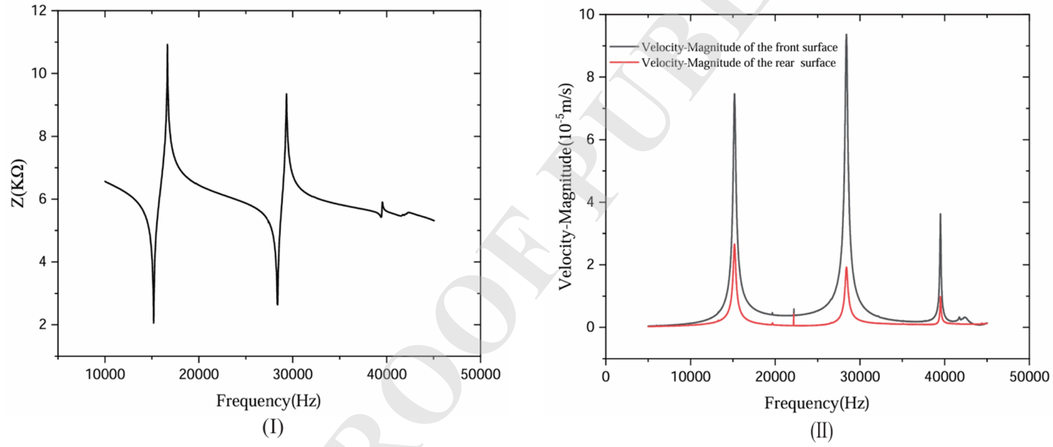

Fig. 17. (I) Experimental electrical impedance frequency response curve result.(II) Experimental longitudinal vibration displacement frequency response results

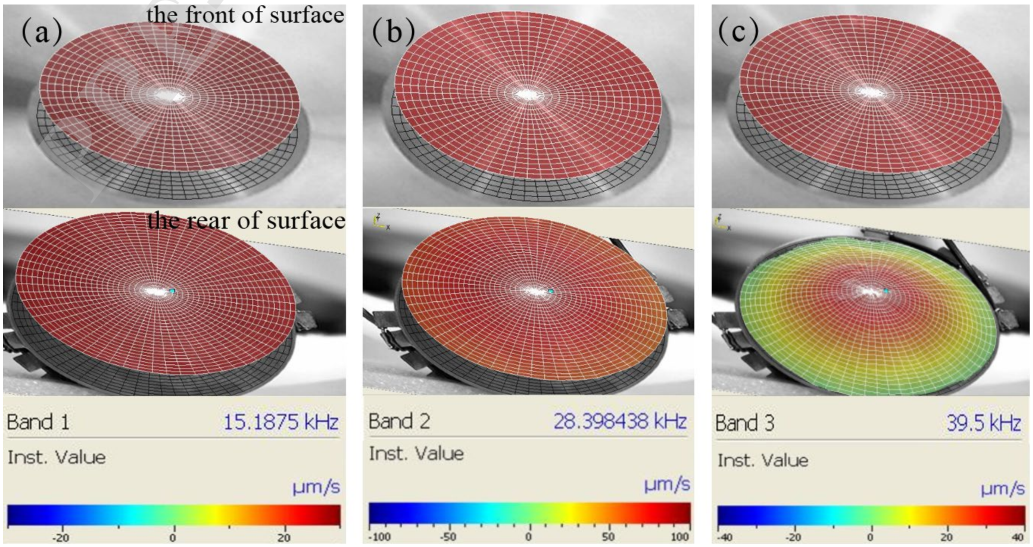

Fig. 18. The longitudinal vibration displacement distributions of the front and rear radiation surface of the transducer: (a) fundamental mode; (b) second mode; (c) third mode

The vibration velocities at the metal block end face and conical output terminal of the transducer were measured using a Polytec laser vibrometer. Fig. 17 illustrates the experimental setup and frequency-dependent longitudinal vibration velocity curves of the front and rear radiation surfaces. The longitudinal vibration displacement distributions are presented in Fig. 18. The first two longitudinal vibration modes exhibit relatively pure characteristics, while the third mode demonstrates coupling vibration effects caused by the larger transverse dimension at the rear end. Nevertheless, the front end maintains satisfactory longitudinal vibration output. The effective electromechanical coupling coefficients and velocity amplification ratios were calculated using $k_{eff}=\sqrt{(1-(\frac{f_r}{f_a})^2)}$ and $M=\left|\frac{v_b}{v_f}\right|$, with comparative results from theoretical, simulated, and experimental approaches listed in Table 5 , respectively, k_t, k_s, k_m and M_t, M_s, M_m denote theoretical, simulated, and measured values.

Table 5. Theoretical, simulated and measured effective electromechanical coupling coefficient and velocity amplitude magnification of the multi-frequency mode transducers.

Mode	k_t	k_s	k_m	M_t	M_s	M_m
Fundamental	0.571	0.447	0.412	2.403	2.68	2.87
Second	0.527	0.277	0.256	3.34	3.68	4.86
Third	0.137	0.036	0.081	4.77	3.54	3.68

As shown in Table 4, the theoretical, simulated, and experimental values for the first two resonant/anti-resonant frequencies show excellent agreement. However, a larger discrepancy is observed for the third-order frequency, where the theoretical value deviates significantly from both the simulated and experimental results. This discrepancy arises because the theoretical model is based on one-dimensional analysis theory, which neglects the influence of transverse vibrations. As the mode order increases, the impact of transverse coupling effects becomes progressively more significant, leading to increased error. Furthermore, discrepancies between the simulated and experimental values exist due to inevitable deviations of the actual material parameters from their nominal values, combined with the neglect of bolt stress effects in the simulation.

As shown in Table 5, the simulated and experimental values of the effective electromechanical coupling coefficient exhibit good agreement, while the theoretical values are consistently higher. This discrepancy arises because the theoretical model neglects dielectric losses and assumes idealized fixed boundary conditions. The experimental velocity amplification ratio for the second mode is significantly higher than both theoretical and simulated values. This occurs because the measured resonant frequency is lower than theoretically predicted, indicating that the actual system stiffness is lower than anticipated. This frequency likely approaches the transducer's true optimal resonant point, where the vibration phase matching between the piezoelectric ceramic stack and metal blocks is improved, resulting in enhanced amplification efficiency. Conversely, the theoretical amplification ratio for the third mode substantially exceeds both simulated and experimental values. This overestimation stems from the theoretical assumption of perfectly rigid metal blocks, whereas at higher frequencies, material compliance and micro-slip at connections become significant, leading to overestimated amplification performance. The remaining amplification ratios show good consistency across all three methods.

5. Conclusions

This paper study on the multi-modal vibration characteristics of a longitudinal cascaded sandwich transducer incorporating a conical horn. Through theoretical and simulation analyses, the influence of key structural parameters on performance was determined, specifically the output radius of the second-stage, the relative position of the variable cross-section of two sets of piezoelectric ceramic sandwich structures, and the spacing between the two sets of piezoelectric ceramics. Optimal transducer dimensions were derived and subsequently validated experimentally. Furthermore, a hybrid configuration combining PZT-8 ceramics with relaxor ferroelectric single crystals was proposed, revealing the impact of piezoelectric material selection on performance metrics. The established optimization methodology holds guiding significance for multi-mode transducer design, while the optimized transducer demonstrates promising application potential in high-power ultrasonic systems. The principal conclusions are as follows:

1. Reduced output radius of the second-stage facilitate concurrent maintenance of substantial effective electromechanical coupling coefficients in first- and second-order longitudinal vibrations, with third-order effective electromechanical coupling coefficients simulations revealing minimal values within smaller radius ranges. This configuration simultaneously enhances first-order vibration velocity amplification ratios while diminishing higher-order responses.

2. The relative positioning of variable cross-section piezoelectric stacks demonstrated negligible influence on operational parameters.

3. Minimized inter-stack spacing proves advantageous for concurrently improving both effective electromechanical coupling coefficients and velocity amplification ratios in primary vibration modes, presenting critical design considerations for practical implementations.

4. Substitution of conventional ceramics with relaxor ferroelectric single crystals in right-side configurations yields enhanced effective electromechanical coupling coefficients

without compromising velocity amplification. Bilateral substitution achieves substantial effective electromechanical coupling coefficients improvement at the expense of reduced amplification ratios, offering flexible material selection strategies for application-specific requirements. These findings establish a methodological framework for performance-adaptive transducer design in high-intensity ultrasonic applications.

Acknowledgment

This work was supported by the National Natural Science Foundation of China (Grant Nos. 12104369 and 12174004), the Key Research and Development Project of Shaanxi Province in China (No. 2025SF-YBXM-470).

References

[1] Shah U. H., Liu X. (2019), Ultrasonic resistance welding of TRIP-780 steel, *J. Mater. Proc. Tec.* 274 116287, https://doi.org/10.1016/j.jmatprotec.2019.116287

[2] Tan W.X., Tan K.W. (2022), Developing high intensity ultrasonic cleaning (HIUC) for post-processing additively manufactured metal components, *Ultra.* 126, https://doi.org/10.1016/j.ultras.2022.106829

[3] Li G., Xu Z., Gong J. H., Li F., Liu Y. B. (2018), Modeling and Experiment of a Small Size Dual Mode Transducer for Underwater Acoustic Communication and Detection, *Acta. Acust United Acust.* 104 947–955, https://doi.org/10.3813/AAA.919260

[4] N. Pokhrel, P. K. Vabbina, and N. Pala (2016), “Sonochemistry: Science and engineering,” *Ultrason. Sonochem.*, vol. 29, pp. 104–128, https://doi.org/10.1016/j.ultsonch.2015.07.023

[5] P. B. Subhedar and P. R. Gogate (2015), “Ultrasound assisted intensification of biodiesel production using enzymatic interesterification,” *Ultrason. Sonochem.*, vol. 29, pp. 67–75, Mar. 2016, https://doi.org/10.1016/j.ultsonch.2015.09.006

[6] F. Chemat, Zill-e-Huma, and M. K. Khan (2011), “Applications of ultrasound in food technology: Processing, preservation and extraction,” *Ultrason. Sonochem.*, vol. 18, no. 4, pp. 813–835, https://doi.org/10.1016/j.ultsonch.2010.11.023

[7] Li J. Q., Zheng J. D. (2023), Two-dimensional composite multi-scale time–frequency reverse dispersion entropy-based fault diagnosis for rolling bearing, *Nonlinear Dyn.* 111: 7525–7546, https://doi.org/10.1007/s11071-023-08250-y

[8] Roland R. (2024), Improving Output Performance of the Ultrasonic Multicell Piezoelectric Motor by Development the Multi-Rotor Structure, *IEEE Access (Volume: 12).* 32080 – 32088, https://doi.org/10.1109/ACCESS.2024.3370560

[9] Jiang C. R., Cheng S. N., Shen Z., Jin L. (2024), Design and analysis of impedance matching for a radial standing wave piezoelectric ultrasonic motor, *Rev. Sci. Instrum*. 95, 015003, https://doi.org/10.1063/5.0180662

[10] Lin S. Y. (2009), Analysis of Multifrequency Langevin Composite Ultrasonic Transducers, *IEEE T. Ultra. Ferr.* 56 1990-1998,

http://dx.doi.org/10.1109/TUFFC.2009.1275

[11] Kuang Y., Jin Y. S., Cochran, Huang Z. (2014), Resonance tracking and vibration stablilization for high power ultrasonic transducers, *Ultra.* 54 187-194, http://dx.doi.org/10.1016/j.ultras.2013.07.001

[12] Du Y. D., Xu L., Zhou G. P. (2020), Vibration characteristics of two-dimensional orthogonal composite sandwich piezoelectric circular transducer, *Sci. Sin.-Phys. Mech. & As.* 51, http://dx.doi.org/%2010.1360/SSPMA-2020-0417

[13] Davari P., Ghasemi N., Zare F., O'Shea P., Ghosh A. (2012), Improving the efficiency of high power piezoelectric transducers for industrial applications, *Sci. Mea. & Tec. Iet.* 6 213-221, http://dx.doi.org/10.1049/iet-smt.2011.0209

[14] Su Q., Liu Y. X., Wang L., Deng J., Li H. (2018), A three-dimensional piezoelectric nanopositioner using a sandwich transducer.[J]. Ceramics International, Vol.44(1): S108-S111, https://doi.org/10.1016/j.ceramint.2018.08.226

[15] Jiang, Z., Wang L., Jin J.M. (2018), A novel robotic arm driven by sandwich piezoelectric transducers.[J]. Ultrasonics, Vol.84(9): 373-381, https://doi.org/10.1016/j.ultras.2017.11.019

[16] Liu S. Q., Yao Y., Lin S. Y. (2009), Radial-torsional vibration mode of disc-type piezoelectric transducer, *J. Mech. Eng.* 45 176–180, https://doi.org/10.1016/j.ultras.2023.107079

[17] Li G., Gong J. H., Wang T., Qiu C. R., Xu Z. (2018), Study on the broadband piezoelectric ceramic transducer based on radial enhanced composite structure, *Ceram. Int.* 44 S250-S253, https://doi.org-/10.1016/j.ceramint.2018.08.101

[18] Meshkinzar A., Al-Jumaily A. (2021), Vibration and acoustic radiation characteristics of cylindrical piezoelectric transducers with circumferential steps, *J. Sound Vib.* 511 116346, https://doi.org/10.1%20016/j.jsv.2021.116346

[19] Watanabe Y,. Tsuda Y., Mori E. (1993), A longitudinal-flexural complexmode ultrasonic high-power transducer system with one-dimensional construction, *Jpn. J. Appl. Phys.* 32 2430–2434, http://dx.doi.org/10.1143/JJAP.32.2430

[20] Lin S. Y., Xu L., Hu W. X. (2011), A new type of high power composite ultrasonic transducer, *J. Sound Vib.* 330 1419-1431, https://doi.org/10.1016/j.jsv.2010.10.009

[21] Lin S. Y., Fu Z. Q., Zhang X. L., Wang Y., Hu J. (2013), Radially sandwiched cylindrical piezoelectric transducer, *Smart Mater. Struct.* 22, http://dx.doi.org/10.1088/0964-1726/22/1/015005

[22] Li F. M., Liu S. Q., Xu L., Zhang H. D., Zeng X. M., Chen Z. J. (2023), Open-slit circular tube piezoelectric ultrasonic transducer with longitudinal bending mode conversion, *Sci. Sin.-Phys. Mech. & As.* 53 114311, http://dx.doi.org/10.1360/sspma-2023-0233

[23] Tressler J., Howarth T. R., Huang D. (2006), A comparison of the underwater acoustic performance of single crystal versus piezoelectric ceramic based cymbal projectors, *J. Acoust. Soc. Am.* 119 879-889, http://dx.doi.org/10.1121/1.2150153

[24] Lin S. Y. (2007), Radial Vibration of the Composite Ultrasonic Transducer of Piezoelectric and Metal Rings, *IEEE T. Ultra. Ferr.* 54 1276-1280, http://dx.doi.org/10.1109/TUFFC.2007.381

[25] Tang Y. F., Chen C., Tian H., Lin S. Y. (2024), Radial vibration analysis for piezoceramic shell-stacked spherical transducer with thick walls, *Smart Mater. Struct.* 33 1454,

http://dx.doi.org/10.1088/1361-665X/ad1e8f

[26] Xu L., Qiu X. J., Zhou J. C., Li F. M., Zhang H. D., Wang Y. B. (2019), A 2D dual-mode composite ultrasonic transducer excited by a single piezoceramic stack, *Sma. Mater. Struct.* 28 025017, http://dx.doi.org/10.1088/1361-665X/aaf275

[27] Hunter G., Lucas M., Watson I., Parton R. (2008), A radial mode ultrasonic horn for the inactivation of Escherichia coli K12, *Ultrason. Sonochem.* 15 101-109, http://dx.doi.org/10.1016/j.ultsonch.2006.12.017

[28] Lin S. Y. (2017), A new type of cascaded high intensity piezoelectric ultrasonic transducers, *J. Shaan. Nor. Univ.* 45 06-22-7, http://dx.doi.org/10.15983/j.cnki.jsnu.2017.06.261

[29] Lin S. Y., Guo H., Xu J. (2018), Actively adjustable step-type ultrasonic horns in longitudinal vibration, *J. Sound Vib.* 419 367-379, http://dx.doi.org/10.1016/j.jsv.2018.01.033

[30] Li G., Qu J. S., Xu L., Zhang X. L., Gao X. Y. (2022), Study on multi-frequency characteristics of a longitudinal ultrasonic transducer with stepped horn, *Ultra.* 121 106683, http://dx.doi.org/10.1016/j.ultras.2022.%20106683

[31] Li G., Lei M., Zhang X. L., Zeng Y., Tang S. J., Shi J. X., Hu L. Q. (2024), Investigation of a cascaded piezoelectric transducer with cone horn for multi-mode power ultrasound application, Phys. Scr. 99 105997, https://doi.org/10.1088/1402-4896/ad6d05